EUROPEAN ORGANIZATION FOR NUCLEAR RESEARCH

CERN-PPE/92-111
21 May 1992

A LARGE AREA OPTICAL IMAGING UV DETECTOR OPERATING WITH TMAE AT 48 °C

J.Baechler[6], M.Bosteels[4], P.Buncic[8], R.Bock[7], A.Di Mauro[2], J.P.Fabre[4], N.Facchini[2], R.Ferorelli[2], W.Heck[5], M.Hoffmann[6], M.Koncul[8], M.LeVine[3,5], A.Ljubicic Jr.[8], E.Nappi[2], G.Paic[7,8], A.Panagiotou[1], F.Posa[2], G.Roland[5], K.Runge[6], A.Sandoval[7], T.Scognetti[2], E.Schmoetten[6], R.Stock[5], G.Tomasicchio[2], G.Vasileiadis[1], D.Vranic[8], M.Wensveen[7].

Univ. Athens[1] - INFN and Politecnico, Bari[2] - BNL[3] - CERN[4]
Univ. Frankfurt[5] - Univ.Freiburg[6]
GSI, Darmstadt[7] - Rudjer Boskovic Inst., Zagreb[8] *

Abstract

We describe the multistep avalanche chamber (MSAC) used in the experiment NA35 at CERN as photon-detector of a Ring Imaging Cherenkov counter (RICH) that upgraded the experimental set-up of a vertex streamer chamber by providing particle identification in the 1.5 - 3.5 GeV/c region.

The chamber design contains some innovative technical solutions to limit the sparking rate and to allow the sensitive area to be larger than the present 50x50 cm^2.

The detector is read-out optically using a CCD camera in conjunction with a system of light intensifiers, since the optical read-out offers a convenient way to record events in a two-dimensional array.

Construction details and test results are discussed.

* Supported in part by the Commission of the European Communities

INTRODUCTION

The Ring Imaging Cherenkov (RICH) counter is an established particle identification technique in high energy physics.
A critical aspect, encountered in exploiting this device, is the efficient detection of the UV photons produced by the Cherenkov effect in the radiator.

A UV photon detector consists mainly of two parts :

- the photocathode which converts photons into photoelectrons
- the photoelectron detector which detects the photoelectron by gas amplification.

Although several types of photocathode may be considered : photosensitive gases with low photoionization threshold (TMAE or TEA) and recently studied CsI films, our choice was TMAE due to the particular geometry of the proposed photodetector and the need to use C_6F_{14} as Cherenkov radiator which absorbs UV light of energy larger than the photoionization threshold of TEA (7.5 eV).

Concerning the photoelectron detector, two solutions have been developed so far : one is the charge collection, the other is the detection of visible light emitted by the photoelectrons (after multiplication).

Although the first alternative is more comfortable regarding the detector requirements (multiplication in the range 10^4 - 10^6), however the electronic readout is directly coupled to the electron multiplying device thus making it sensitive to any malfunction (sparking, large ionization phenomena etc.) occurring in the detector itself. On the other hand, the optical read-out where the end plane of the electron detector is viewed by a camera, achieves a complete separation of the electron multiplication and light production regions from the recording device. The price to be payed is a higher electron multiplication (10^7) in the chamber in order to generate sufficient light.

Small size devices with optical read-out have been tested succesfully with Multistep Avalanche Chambers MSAC (1,4) as photoelectron detector.

The MSAC was developed by Charpak et al. (2) in the early 80s with the aim to overcome the operational limits of multiwire proportional chambers when used to detect high fluxes of particles.

The detector concept relies on photon mediated transfer of ionization and it is realized by two distinct and separate charge amplification regions in order to obtain high gains. A wire plane electrode "gate", in between the two amplification stages makes the MSAC a device where the full charge amplification is achieved only when an external selected trigger enables the gate electrode. When the gate is open, the electron avalanches produced in the first amplification region are permitted to drift toward the second stage.

Vapors of TMAE or TEA are added to the MSAC gas mixture. Their role is twofolds : the low ionization potentials (5.3 eV and 7.5 eV respectively) allow photoionization by Cherenkov photons in the conversion region, and in the last amplification region, the excitation of the same gases caused by electron avalanches, produce light emission that can be detected either directly, in the case of TMAE, or via a wavelength shifter in the case of TEA. In this paper we present an attempt to build a large prototype optically read-out used as a RICH detector in the study of nucleus-nucleus collisions at CERN.

DESCRIPTION OF THE OPERATION OF THE MSAC AND REQUIREMENTS ON ITS PERFORMANCE

A MSAC for the detection of UV photons consists of three distinct parts :

1) The conversion volume, where the UV light enters through a highly UV-transparent window to be converted into electrons via interaction with photosensitive molecules (TMAE in our case).

2) The gas amplification volumes where electron amplification takes place. Usually two of such volumes are provided with a gain of 10^3 each. In these volumes, besides electron multiplication, photon emission takes place via deexcitation of the photosensitive component of the gas mixture.

3) The transfer volume between the two amplification gaps that may be used to incorporate an active gate device.
The requirements on the performance of the whole detector derive from the optimization of the operation of each part.
For best efficiency and minimum depth of the conversion region (to minimize the parallax error) it is necessary to use the maximum concentration of photosensitive vapour. Since TMAE is a non volatile liquid at ambient temperature it is necessary to bubble the gas mixture through the liquid TMAE at the highest temperature possible. To prevent TMAE condensation in the chamber the detector volume should be kept several degrees warmer. This requires that the detector should work reliably at a temperature of 50-60 °C.
For an uniform gas amplification the main requirement is the parallelism of the meshes that define the volumes and their rigidity to avoid deformation under electrostatic forces.

GENERAL DESCRIPTION OF THE MSAC

In order to prevent the effects of the well documented chemical reactivity of TMAE (3), a careful choice of construction materials was done and a long term ageing study was performed on a small prototype (4).

The MSAC consists of 6 machined Stesalit frames of 620x620 mm^2 external size and 520x520 mm^2 internal size with different thickness as shown in fig. 1, packed together and stiffened by two external Stesalit frames supporting the entrance fused silica window* and the exit pyrex window.

All the electrodes, except for the gate, are made of stainless steel cross wire meshes, having 50 μm wire diameter and 500 μm pitch.

The meshes, stretched at 160 kg/m, are soldered on printed boards. Details of this construction phase are reported in the next section.

The gate electrode is made of 520 Cu-Be 100 μm wires, spaced 1 mm apart. These wires are soldered on printed boards with a precision of 0.2 mm and a tension of 200 ± 20 g.

Wires are connected alternately to two independent opposite high-voltage supplies to keep the gate normally closed. Experience shows that a difference of 200 V completely closes the gate (4).

---

* SUPRASIL II, HERAEUS
CORNING 7940

The gas volume of the chamber is closed on the side facing the incoming UV photons by a fused silica window (10 mm thick) that is transparent to Cherenkov photons of wavelength larger than 160 nm (80% of transparency).

Photoelectrons, produced in the 7 mm conversion gap, drift toward the first 4 mm amplification gap where a multiplication of 10^3 occurs. Then the electron cloud transfers into the 20 mm low field drift region with a transmission factor given by the ratio between the value of the latter field and that of the preamplification gap. The thickness of the drift region is governed by the time needed to implement a trigger. In fact, for trigger selected events, opposite polarity pulses are applied to the gate wires to set the potential of the whole electrode to the same value, thus allowing further drift to the 11 mm thick second amplification stage only for the selected electron clouds.

The second amplification gap is chosen larger than the first to increase the probability of excitation of TMAE molecule and, hence, the light yield of the TMAE isotropic emission of 480 nm. The field in the second amplification gap is kept lower than the operational value and the last electrode is pulsed to its full voltage at the time the electrons arrive in the gap. In this way we limited the sparking rate of the chamber.

A pyrex plate, 10 mm thick exit window, closes the gas volume allowing the emitted light to be collected by the imaging system.

CONSTRUCTION DETAILS

To stretch uniformly the stainless steel meshes and to prevent deformation of the finished electrode, we use the following procedure.

Almost 1 m^2 of mesh is stretched and fixed over an expandable mounting frame larger than the supporting one in Stesalit. The final tension of 160 kg/m is set after heating the mesh to a temperature close to the detector operating temperature of 50 °C. The heating is achieved by infrared lamps above the stretched mesh. The mesh, still under stress is soldered on a printed circuit track glued with Araldite to the corresponding Stesalit frame. The role of the track is to allow uniform soldering and to feed the high voltage to the mesh electrode (fig. 2). Precision machining of the Stesalit frames achieves deviations from planarity of less than 50 μm. To avoid any further non-uniformity due to the gluing of printed boards on Stesalit frames, we decided to discard the solution shown in fig. 2a. The mechanically more complicated solution shown in fig. 2b was choosen. In this case the planarity is maintained by the presence of the Stesalit ridge in between the printed board and the inner part of the frame.

An additional advantage of this solution is that the solder flux is prevented from reaching the frame inner wall, where it may cause a reduction in the Stesalit surface resistivity.

All frames are washed with ethyl alcohol and assembled in a dust free room.

Electrostatic attraction, produced by the strong field in the amplification gaps, is alleviated by stretching the meshes at the limit of elasticity and by placing an array of four equidistant spacers between each pair of adjacent electrodes in the gas amplification volumes.

The shape of the amplification regions walls and spacers is critical to prevent voltage breakdown along the edges.

Good results are obtained with 3 mm diameter cylindrical spacers in Stesalit machined with 7 mm diameter thin end caps to increase the sparking path. To reduce the edge effect in the high field regions we have used the so called pushers; a

profile on the frame that pushes the mesh at the required distance from the lower electode but keeps at the edge a larger gap (up to 1 mm), see fig 1.

Because of the difference in thermal expansion coefficients of Stesalit and fused silica, special care was taken in designing the 710x710 mm^2 quartz support frame. At the working temperature of 50 °C, simple gluing of the quartz plate on the Stesalit frame did not fulfill the required gas tightness. Therefore we adopted a technical solution based on mechanical clamping of the plate in between two Viton O-rings placed in grooves machined in the Stesalit frames with an excellent planarity (10 μm tolerance) as shown in fig. 3.

VISIBLE LIGHT RECORDING

The light produced by the avalanches in the UV detector is recorded by a CCD camera of very high single photon detection efficiency. The camera consists of three parts : the objective lens, the three stage image intensifier and the CCD chip. The optimization of the whole chain of optical imaging is essential for a successful operation.

i) The objective

The objective used was a Leitz Noctilux 50 mm/1.0 lens. The large aperture, required for maximal collection of light from the detector, results in a very small depth of field of ± 1 cm. This feature has forced us to focalize using a test pattern localised on a plane just in front of the detector exit window and then to move the lens and the complete camera assembly by the distance from this plane to the last amplification gap where the light is created by the electron avalanches. Such a procedure is necessary because no pattern can be inserted in that gap to focalize on.

ii) The image intensifier

The image intensifier consists of three stages : an electrostatic image intensifier at the entrance, a microchannel plate image intensifier and finally a tapered electrostatic image intensifier to match the size of the second stage of the chain to the CCD chip dimension. The main characteristics of each of the three stages are shown in table 1. All the image intensifiers in the chain are equipped with input and output optical fibre face plates. The coupling of the CCD to the chain was also done using an optical fibre plate.

Table 1
Dimensions and performances of the image intensifiers

	VARO 1248	ITTF4413	DEPXX1310B
Entrance Diam. (mm)	40	40	40
Exit Diam. (mm)	40	40	13
Light gain ph/ph	20	$12x10^3$	7
Input limiting resolution lp/mm (50 % MTF)	20	6	10
Magnification	1	1	13/40

Given the parameters from table 1, the resolution of the image intensifier chain can be calculated. This figure determines the minimum two photon separation that can be reached.

The resolution of an image intensifier is given by the expression (5)

$$\sigma \simeq 0.187/R \text{ (mm)} \qquad [1]$$

where R, the limiting resolution in line pairs per millimeter of the chain, is given by

$$R^{-1} = [\Sigma 1/(MR_i)^2]^{1/2} \qquad [2]$$

where R_i is the input limiting resolution for individual stages, and M is the magnification of the chain achieved up to the ith intensifier including its own magnification. From relation [1], the parameters from table 1 and taking in account the resolution of the lens (11 lp/mm), the CCD (20 lp/mm), we get for our case sigmaopt = 50 μm at the entrance window of the chain. Transferred to the object plane in the detector with a magnification of 21, this corresponds to a sigmaopt = 1.0 mm. This optical resolution is of the same order of magnitude as the intrinsic width of the avalanche caused by the single photoelectron, and is therefore well matched to the performance of the detector.

The stacking sequence of the image intensifiers was chosen according to various criteria such as : single photon efficiency, spatial resolution, and signal to noise ratio.

The schematic of the camera is shown in fig. 4. The last element in the chain is an image intensifier that serves to match the 40 mm diameter of the MCP to the 11 mm diagonal size of the CCD chip. The solution of using an image intensifier instead of an optical fibre taper was adopted considering the lifetime of the Microchannel plate. Namely the life cycle of an MCP is primarily limited by the current it has to deliver. This is due to the fact that, during the electron multiplication, the secondary electrons acquire an energy of 50 to 100 eV between each multiplication step. This energy is sufficient to dislodge the gas molecules trapped in the channel surface and some of them are ionized and accelerated thus causing the bloom effect resulting in gain loss (6). Therefore it seems wise to have a lower multiplication in the microchannel plate and use an image intensifier with a gain 5-10 instead of a taper whose transmission is of the order of $0.6 \times M^2$.

Camera gating

To minimize the background of the image intensifiers it is important to intensify with the optoelectronic chain only during the time when the gate is open in the UV detector and light effectively produced. The electronic shutter operates with the application of a voltage pulse of -180 V to the photocathode of the MCP image intensifier for the time we want the camera active. In our case the voltage pulse was chosen to last 2-3 μs.

The CCD read-out and the data acquisition system

The CCD coupled to the image intensifier assembly is a 576 x 384 pixel device (Thomson-CSF TH 7863) with pixels size of 23x23 μm^2. The CCD consists of 2 zones of equal area. One is optically sensitive; the second is used as a memory zone, each zone consists of 288 x 384 pixels. Images acquired in the sensitive zone are transferred to the memory zone in approximately 500 microseconds. The frame

transfer imposes a system dead time, transfer is accomplished one image line at a time. However, the readout of the memory zone processes the pixels serially. Thus the readout is considerably slower than the transfer, requiring some 20 msec. The CCD management (transfer plus readout) is handled by a commercially available drive module (Thomson-CSF TH7966-3). The analog signal corresponding to each pixel is converted to an 8-bit digital value by a VME-resident Data Cube digitizer board (MaxScan). This board can be programmed to handle a large variety of camera formats, and has the capability of performing real time signal processing operations like thresholding, lookup-table substitutions. These capabilities are used here to replace all sub-threshold values with zero, making the subsequent processing much more efficient. The resulting data are transferred to a second VME board (Data Cube ROIStore) via a Data Cube front-panel proprietary bus. The ROIStore module provides dual-ported buffering for up to 4 frames. Its high speed front-panel port allows real-time storage of image data. The data acquisition software reads the frames stored in the ROIStore via the VMEbus.

The data acquisition system consists of two parts. The heart of the system is in VMEbus, whereas the user interface (commands and data display) is implemented on an Apollo 10000 workstation.

The VMEbus system is managed by a 20 MHz 68030 CPU (Motorola MVME147-SA) equipped with 8 MBytes of RAM, SCSI interface, and Ethernet. The SCSI bus contains a 160 MByte hard disk, a streamer tape, and an Exabyte 8200 8mm tape drive used for recording data. The VME crate contains a CAEN V262 NIM input-output module to provide the computer-busy logic. The software environment for the MVME147 is Microware's OS9 operating system. This real-time, event-driven, multi-tasking environment is based on a native development environment (compiler, assembler, debuggers, editor) and provides real-time performance adequate for this application. The basic tasks for this application : reading the ROIStore memory, managing the busy logic, recording data on 8 mm tape, providing sample events for remote display, and accumulating histograms, are controlled either from an utility running on a local terminal, or remotely via individual TCP/IP socket interfaces to each of the tasks involved.

Connections to these sockets can be made, for example, from a workstation in order to request sample events, or to start or stop a run.

The data acquired from the CCD are handled by a buffer manager which allows events created by a "producer" (ROIStore readout) task to be made available to several "consumer" tasks (tape logging and display). The availablity of this utility facilitated the implementation of a data acquisiton system.

The user interface, running on an Apollo 10000 workstation, called WOnDER (Windows Online Display of Events from RICH), is implemented as an X-windows client, thus providing control and display in a single application.

DISTORTION CORRECTIONS

The distortion corrections in a CCD camera are an important element. In our case the camera operated in the fringe field of a magnet and, in spite of a mu-metal shield, the magnetic field introduced additional distortions. Such distortions have to be measured in full operating conditions i.e. with the magnetic field and the full voltages on the image intensifiers. In practice, the last condition presents a very difficult obstacle. It means that the correction grid should have very low luminosity in order to allow full intensification. After several trials we found that the best solution was to adopt the following scheme. A grid pattern was machined

with 20 μm precision on a plexiglass plate. The grooves were 500 μm deep and 500 μm wide. In the grooves optical fibres were inserted, the fibres were connected together in a bundle and illuminated with a lamp. The sideways light leakage from the fibers was sufficient to achieve good grid measurements at full voltage on the camera.

Heating system

The operation of the UV detector with the gas mixture containing TMAE vapour is critically dependent on the stability and uniformity of the operating temperature. The heating system has to provide constant temperature to TMAE bubbler, gas circuit and detector assembly.

The bubbler and gas circuit heating is obtained by means of temperature regulated heating tapes.

- Detector assembly heating

We have first tried a forced air circulation, but the insufficient heat capacity makes such a system difficult to operate safely over long periods of time. Finally we opted for a water circuit heating solution. The detector is surrounded by copper plates with brazed on copper tubes through which warm water circulates. The heating panels are insulated on the outer side. The circuit we are describing is particular in the sense that it is a "leakless" circuit operating under static underpressure. This feature increases the system reliability since accidental leaking is prevented and disconnection of the heating panels during operation is easy. The filling procedure of the system illustrated in fig. 5 is as follows :

- lower tank : the filling is achieved through the electrovalve (EV/H20) controlled by two level monitors.
- upper tank : on powering the circuit , the vacuum pump and the valve EV/VP are activated so that the air in the circuit is evacuated creating an underpressure in the system that sucks up the water from the lower tank into the upper tank. When the level controlled by the monitors is reached in the upper tank, the vacuum pump is stopped, the valve closed thus isolating the circuit and simultaneously bringing the pump to air. Should the pressure in the circuit, controlled by the manometer, rise, the vacuum pump is activated again.

The water circulation is ensured by circulator. The electrical heater in the lower tank is controlled by a CAL regulator coupled to a Pt100 temperature sensor. A mechanical thermostat disconnects the heater power supply in case of malfunction of the CAL regulator. The heater circuit is also broken by lack of water in the system.

To purge the circuit, the system is disconnected from power and the air is let in through the mechanical purge valve. The water then flows to the lower tank and is evacuated through the drain.

Long term stability of ± 0.5 °C has been observed with the detector at 55 °C over several weeks.

Performance of the UV-detector

Measurements to evaluate the spatial resolution and the single-avalanche features were performed using a pulsed deuterium lamp. The lamp light illuminated the device through 24 holes (300 μm diameter), drilled in a thin vetronite plate along two concentric circular patterns, the inner one with a diameter of 100 mm and the outer one with a diameter of 220 mm (fig. 6).

The MSAC was initially operated with two different gas mixtures : helium(93%)-ethane(7%) and helium(93%)-methane(7%) both with TMAE at 48°C to study the respective detector behaviour. The gas circulation system is shown in fig. 7.

From the comparison of the operating voltages, needed to produce the same light yield from the chamber with the two mixtures, shown in table 2 and best stability of operation with lower fields and less sparking rate convinced us to keep He/CH_4 and therefore the test results will be referred only to the above gas mixture.

Table 2

Operating voltages to the electrodes identified by the numbers in fig.1. The two gas mixtures are operated with TMAE at 48° C.

	He/CH4	He/C2H6
HV1	-4.6 KV	-5.4 KV
HV2	-3.98 KV	-4.8 KV
HV3	-2.0 KV	-2.5 KV
HV4	-0.59 KV	-0.66 KV
HV5	GROUND	GROUND
HV6	+3.08 KV(+0.45 KV)	+3.25 KV(+0.45 KV)

In order to study the detector performance at the single UV photon level, the light intensity was attenuated by a set of Aclar 22 A foils. Fig 8 shows the relative frequency of avalanches from UV photons passing through four adjacent holes. The Poissonian fit to the data, clearly indicates that the detected light stemm from single photoelectron.

Intensity distributions in the CCD regions around light blobs are shown in fig. 9. The coordinates on the horizontal plane indicate the position of the pixels and the vertical axis corresponds to the luminosity. Two classes of blobs are easily recognizable. The first one consists of a very bright central peak surrounded by pixels whose intensity is slowly decreasing towards the periphery (fig. 9a), this class of blobs is superimposed on a random background of very low intensity due to CCD noise. The second class, shown in fig. 9b, represents spike-like structures whose peak intensity is always less than 20. The intensity distribution for all the pixels from all the events of a certain run is shown in fig. 10. The kink at about 20 clearly indicates that the mentioned second class of blobs has luminosities falling down very steeply. We therefore determine luminosity 20 as the noise mean level and set an intensity cut at 20 for the subsequent event analysis. The photon spots are identified by a peak finding and cluster association procedure. Peaks are found by scanning all the CCD image with a 3x3 pixels mask : a peak candidate is a pixel with the highest luminosity within the mask surrounded by pixels whose average luminosity is larger than 30 and larger than 1/10 of the peak luminosity. If the blob has several pixels in saturation, then the peak is associated to the one surrounded by pixels with the highest average luminosity. The clusters are found associating the pixels in the 3x3 mask to the closest peak. If the pixels are equidistant from two or more peaks, they are associated to the highest intensity peak. The position of the cluster is defined by its centroid. When all centroids are found, the typical image consists of spots corresponding to the two ring-like patterns drilled in the lamp mask and sometimes of spurious hits that most probably are due to photon feed-back (fig. 11). The cluster intensity distribution is shown in fig. 12. The peaked-

shape distribution indicates the good efficiency of the device for the single-photon detection. The cluster luminosity is strongly dependent on the charge transfer ratio between the preamplification and the drift gap electric fields, more specifically, the percentage of clusters in saturation goes from 0 at 16% of transfer to 33 at 20 % of transfer, the centroid luminosity, outside the saturated clusters, is slightly varying as shown in fig. 13. The chamber electronic gain, checked comparing the light responses from different holes in the lamp mask, is uniform within 3 %. From fig. 12 we estimate from the cutoff occurring at total cluster luminosity = 400 that the efficiency of the chamber for single photoelectron detection ranges from 0.7 ÷ 0.75.

Spatial resolution

The spatial resolution of the detector has been calculated using the spot intensity centroid distributions. The centroid position is influenced by the intrinsic spatial resolution of the whole detector - optical read-out system, by the parallax in the conversion gap due to the oblique incidence of the photons entering the quartz window, (see fig. 14 for the respective position of the holes and UV flasher), and by the chromatic aberration due to the spread in the UV lamp spectrum. The effect of the parallax is clearly seen in fig. 15 where the centroid distributions relative to three different hole positions in the lamp mask along two orthogonal axes and at 45° to them respectively, are represented. Considering that 75 pixels are equivalent to 134 mm in the MSAC plane, the spatial resolution calculated with the previous method is better than 800 μm taking in account that the holes crossed by the UV light have a diameter of 300 μm, and that the localization of the emitting point in the sparking gap is not point like.

Double hit resolution

The double hit resolution has been deduced from the distribution of the cluster size. In fact we can assume that a Townsend avalanche is quite symmetric in the plane perpendicular to the electric field and then the average diameter of a cluster can be considered the measure of "double hit resolution" of the detector. From fig. 16 a value of 3 pixels corresponding to 5 mm has been calculated.

CONCLUSIONS

We have shown that a large scale MSAC detector can be optically readout. Its feasibility to efficiently detect single UV photons and then to equip a ring-imaging Cherenkov device has been proved. Construction details have been reported, some of them are based on innovative technical solutions to improve the realibility and operational stability of large sensitive area detectors. With the adopted image intensifiers, but using a CCD of 512x512 pixels, the present results indicate that one optical chain can cover a photodetector as large as 1x1 m^2.

ACKNOWLEDGEMENTS

We are grateful to Dr. W.Dominik, Dr. F.Sauli, Dr. N.Solomey, and Miss M. Gruwe for many useful discussions. We wish to thank specially Mr. M.Mongelli for designing and making the construction drawings of the detector. We are grateful to Mr. E.Barbarito and Mr. M.Perchiazzi for their skillful work in assembling and operating the MSAC. The unvaluable help of Messrs. J.Dupont and G.Trouiller in designing and building the optical system is also acknowledged.

REFERENCES

[1] G.Charpak et al., IEEE TRANS. Nucl. Sci. NS-35(1988) 237
A.Breskin et al., IEEE TRANS. Nucl. Sci. NS-35(1988) 404
A.Breskin et al., Nucl. Instr. and Meth. A237(1988) 698

[2] G.Charpak et F.Sauli, Phys. Lett. 79B(1978) 523
R.Bouclier et al. Nucl. Instr. and Meth. 205(1983) 403-423

[3] R.T.Rewick et al., SLAC-PUB-4115 (1987)

[4] G.Vasileiadis et al., Nucl. Instr. and Meth. A289(1990) 618

[5] A.Breskin et al., Nucl. Instr. and Meth. A286(1990) 251-261

[6] Illes P.Csorba, Image tubes, Howard W. Sons & Co, Inc. 1985

FIGURE CAPTIONS

Fig. 1 Schematic structure of the MSAC. Electrodes identified by the numbers 1, 2, 3, 5, 6 are crossed wire meshes, while 4 is a plane of parallel wires "gate electrode". The photoelectron created in the 7 mm gap "conversion gap", is amplified in the 4 mm preamplification region and drifted from the 20 mm gap to the 8 mm gap if the gate electrode is equipotential at the time the electron avalanche drifts. The last amplification is provided by the electric field in the 11 mm gap delimited by electrodes 5 and 6.

Fig. 2a, 2b
The two possible ways of fixing the stainless steel mesh to the Stesalit frame. The scheme shown in 2a is mechanically easier than in 2b that gave more satisfactory results since the presence of the Stesalit ridge in between the printed board and the inner part of the frame provides a planarity of the precision achieved by the Stesalit frame.

Fig. 3 Detail of the frame supporting the quartz window : the UV transparent plate is clamped in between two Viton O-rings placed in grooves machined in the Stesalit frames.

Fig. 4 Schematic of the optical read-out system : a mirror, placed at 45 with respect to the detector exit window, reflects the produced light to the imaging system. A Leitz-Noctilux objective focalizes the image on the image intensifier complex that consists of three stages : an electrostatic intensifier (VARO) at the entrance, a microchannel plate (ITTF4413) and finally a second electrostatic intensifier (DEPXX 1310B). The CCD management is handled by the driver Thomson-CSF TH7966-3 whose analog output corresponding to each CCD pixel is converted to an 8-bit digital value by a VME-resident DATA CUBE digitizer board.

Fig. 5 Schematic of the chamber heating system. The circuit operates under static underpressure. The vacuum pump and the valve EV/VP are activated switching on the main power. The air in the circuit is evacuated creating an underpressure in the system that sucks up the water from the lower tank into the upper tank. The filling is achieved through the electrovalve EV/H20 controlled by two level monitors.

Fig. 6 Details of the copper plate used to mask the UV flasher light. The two circular patterns are shown.

Fig. 7 Schematic of the gas circulation system.

Fig. 8 Frequency distribution of avalanches from UV photons that cross four adjacent holes in the mask. The superimposed Poissonian fit indicates that the detected light stemm from single photoelectron.

Fig. 9a, 9b
Lego plot distribution of the CCD regions around the blobs. Two class of blobs are shown : the first has clusters with a two dimensional gaussian intensity distribution (9a), the second class has spike-like structures of low peak intensity (9b) later identified as noise.

Fig. 10 Pixel intensity distribution. The kink at 20 set an intensity cut for the event analysis.

Fig. 11 Centroid positions of avalanches in the CCD image.

Fig. 12 Cluster intensity distribution.

Fig. 13 Average luminosity of the not saturated clusters vs. charge transfer.

Fig. 14 Schematic of the lamp mask showing the respective position of the holes and the UV flasher.

Fig. 15 Distributions of the centroid positions relative to three different hole orientations in the lamp mask. The effect of the parallax is seen in the holes along the orthogonal axes, the hole at 45 shows the parallax effect in both projections. The spots not belonging to the peak are due to photon feedback and were not taken into account in the fits.

Fig. 16 Cluster size distribution.

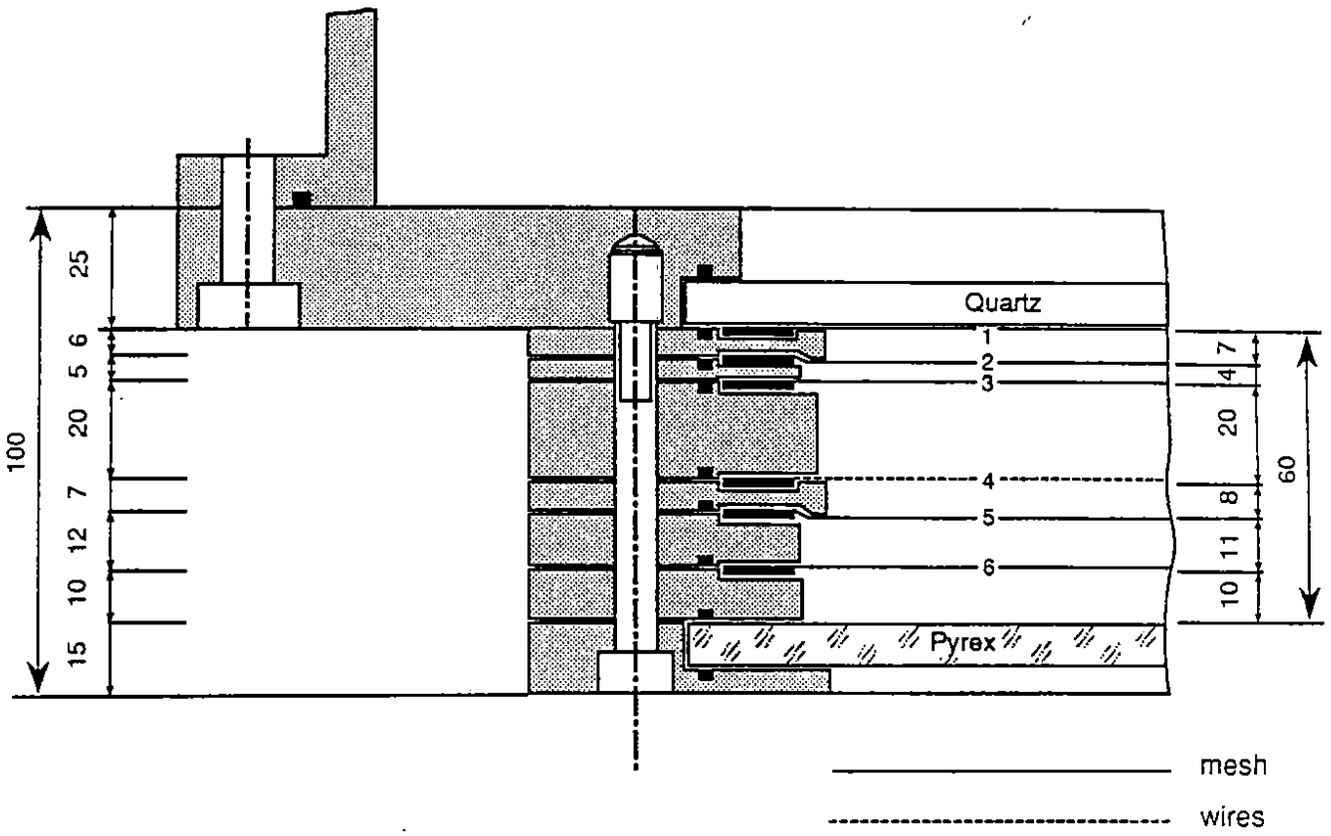
100
25
6
5
20
7
12
10
15
Quartz
1
2
3
4
5
6
Pyrex
7
4
20
8
11
10
60
mesh
wires

Fig. 1

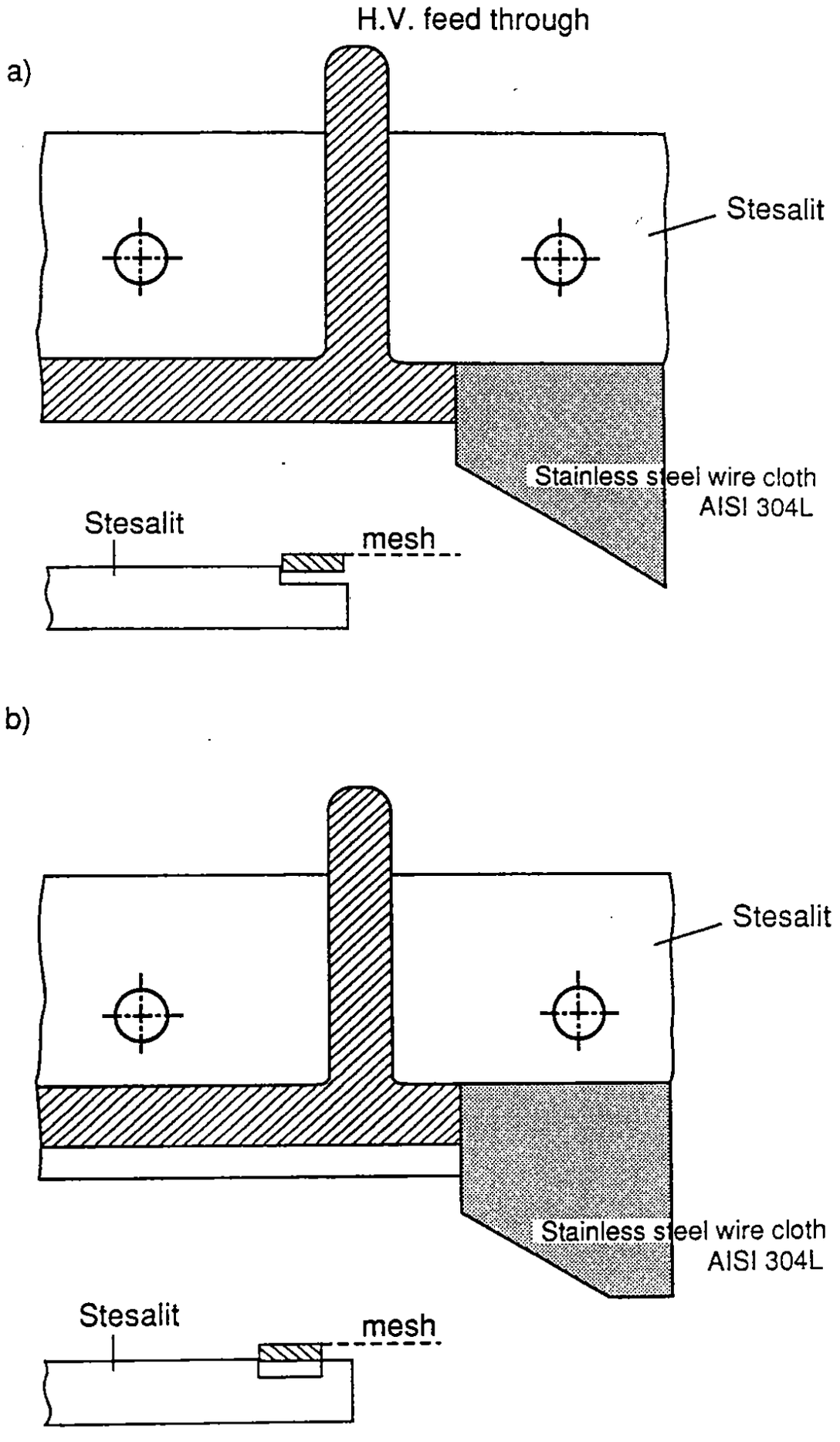
a)
H.V. feed through
Stesalit
Stainless steel wire cloth
AISI 304L
Stesalit
mesh
b)
Stesalit
Stainless steel wire cloth
AISI 304L
Stesalit
mesh

Fig. 2

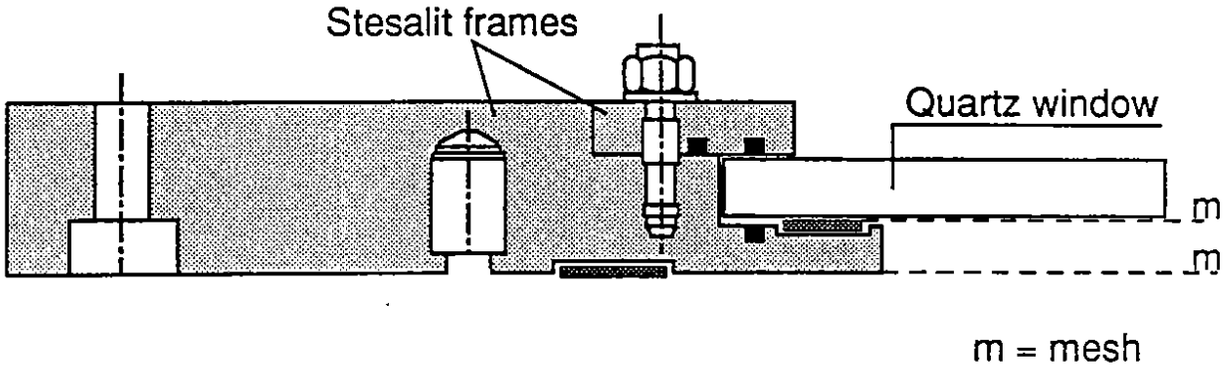

Fig. 3

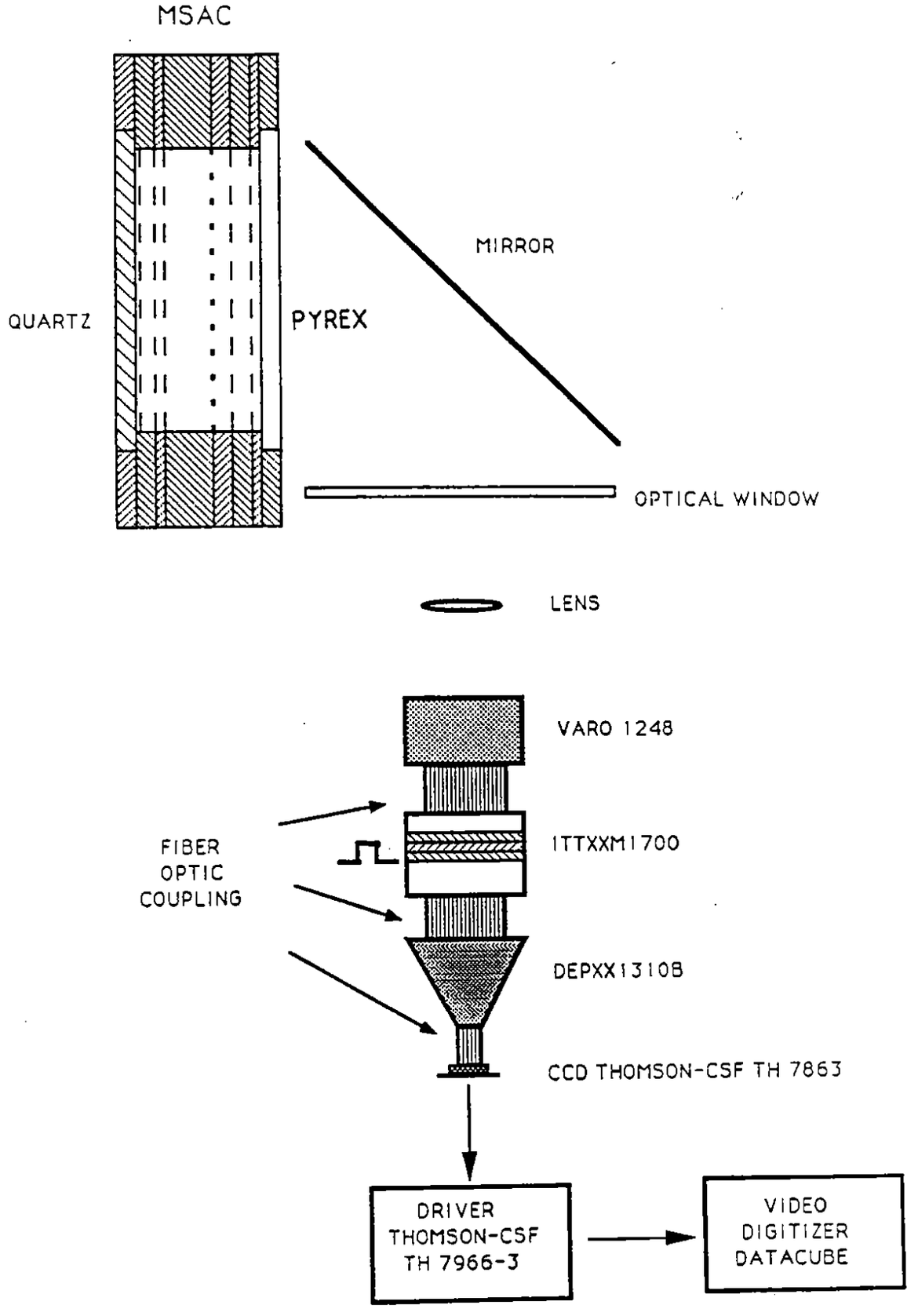
MSAC
MIRROR
QUARTZ
PYREX
OPTICAL WINDOW
LENS
VARO 1248
FIBER
OPTIC
COUPLING
ITTXXM1700
DEPXX1310B
CCD THOMSON-CSF TH 7863
DRIVER
THOMSON-CSF
TH 7966-3
VIDEO
DIGITIZER
DATACUBE

Fig. 4

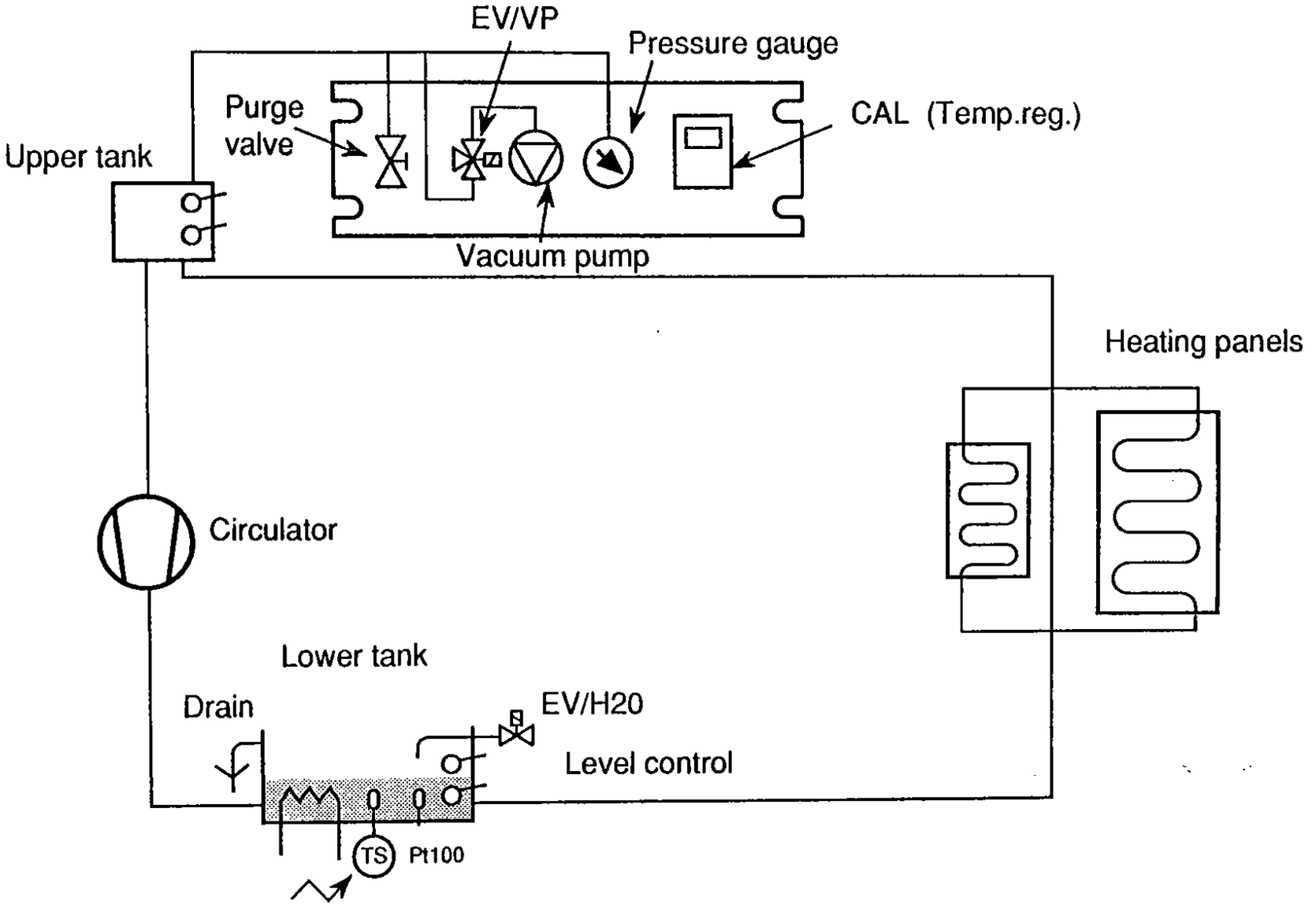
EV/VP
Pressure gauge
Purge valve
CAL (Temp.reg.)
Upper tank
Vacuum pump
Heating panels
Circulator
Lower tank
Drain
EV/H20
Level control
TS
Pt100

Fig. 5

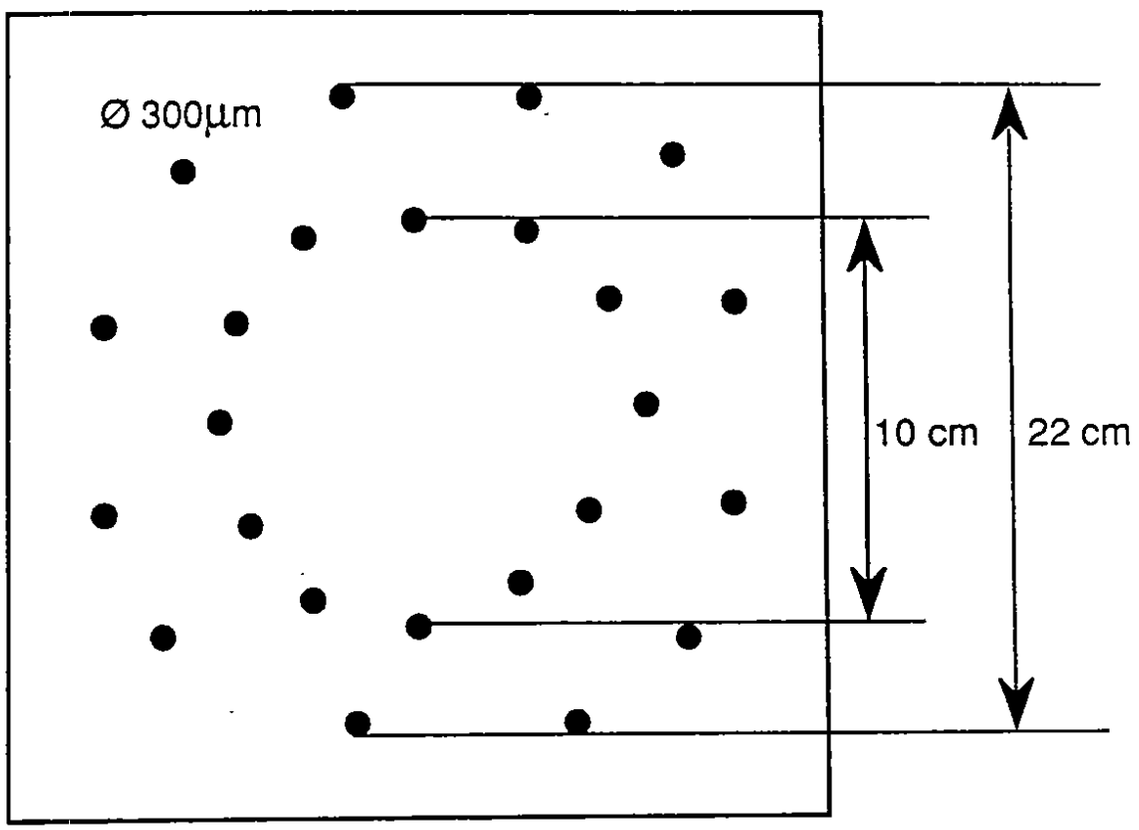

Fig. 6

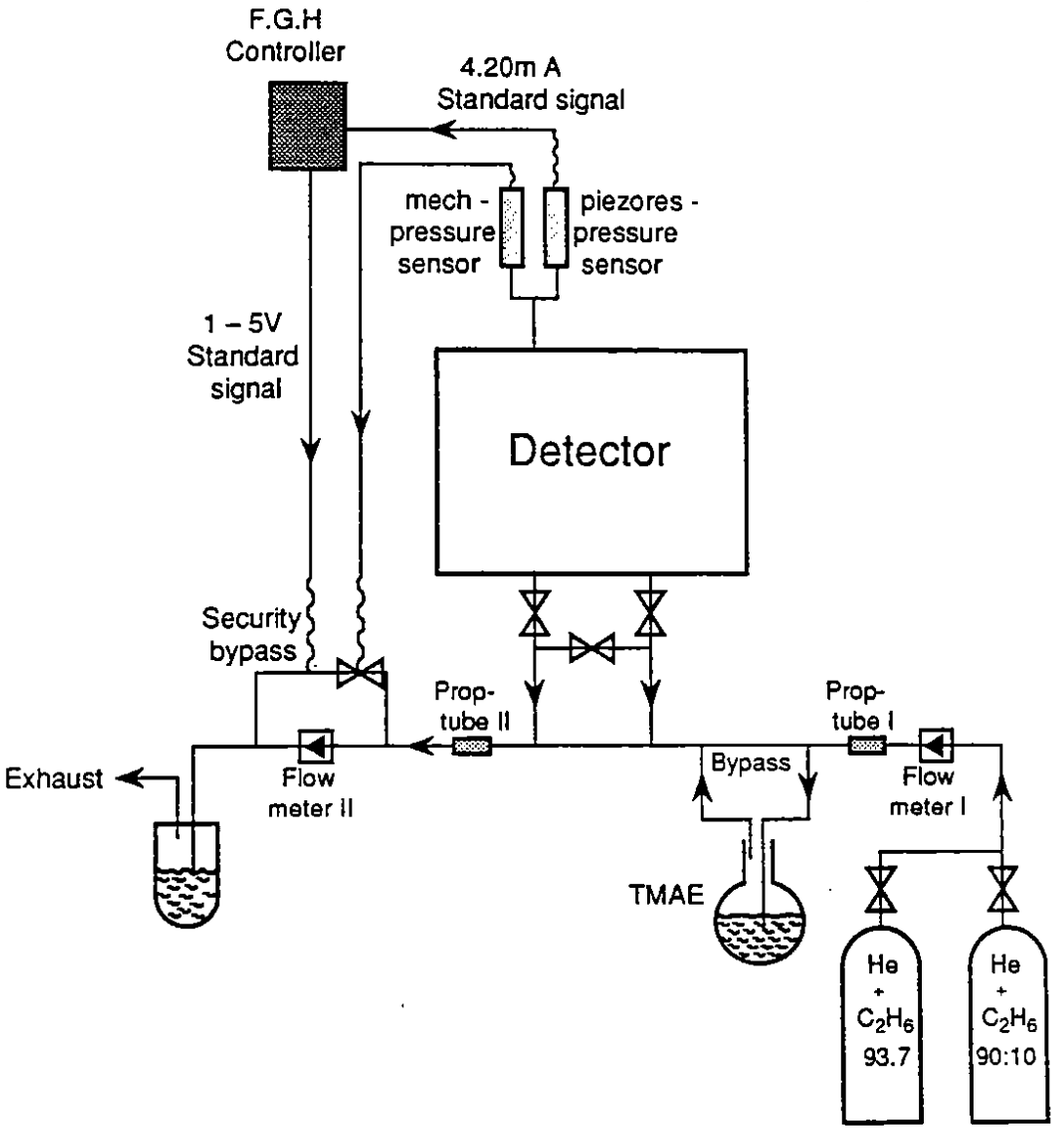
F.G.H
Controller
4.20m A
Standard signal
mech -
pressure
sensor
piezores -
pressure
sensor
1 – 5V
Standard
signal
Detector
Security
bypass
Prop-
tube II
Prop-
tube I
Exhaust
Flow
meter II
Bypass
Flow
meter I
TMAE
He
+
C_2H_6
93.7
He
+
C_2H_6
90:10

Fig. 7

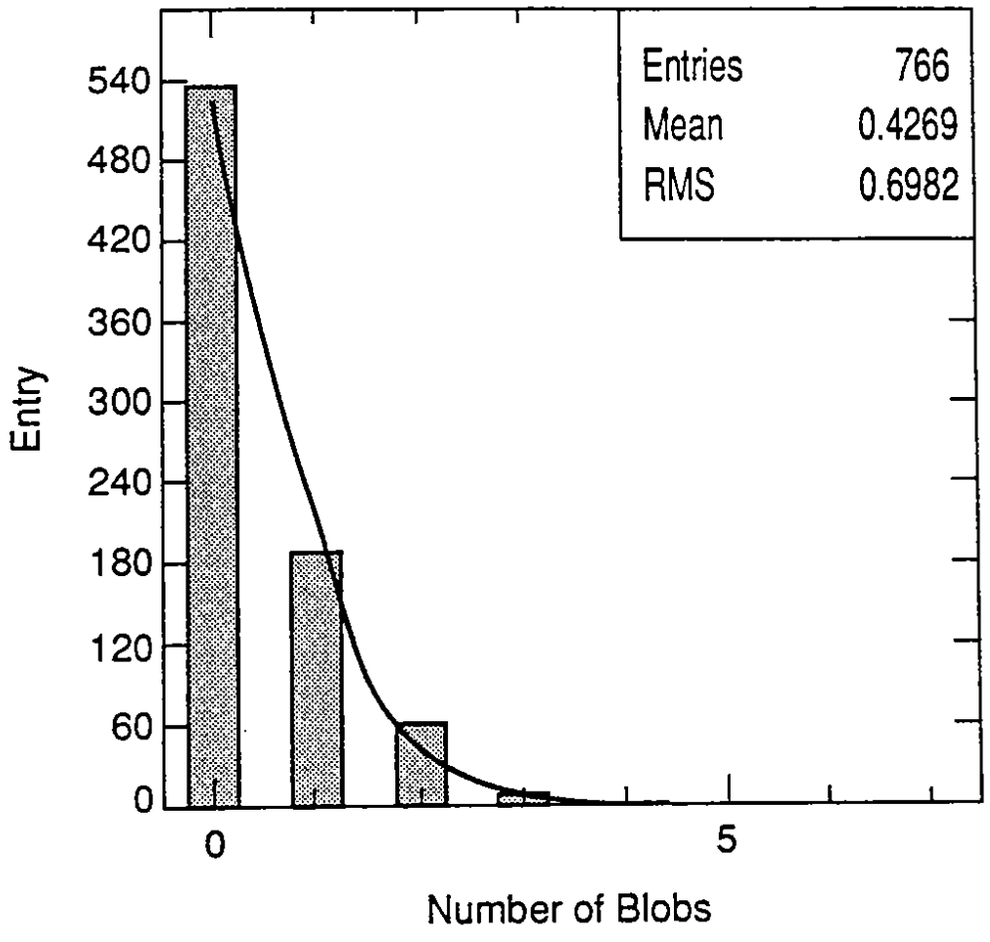
Entries 766
Mean 0.4269
RMS 0.6982
540
480
420
360
300
240
180
120
60
0
Entry
0
5
Number of Blobs

Fig. 8

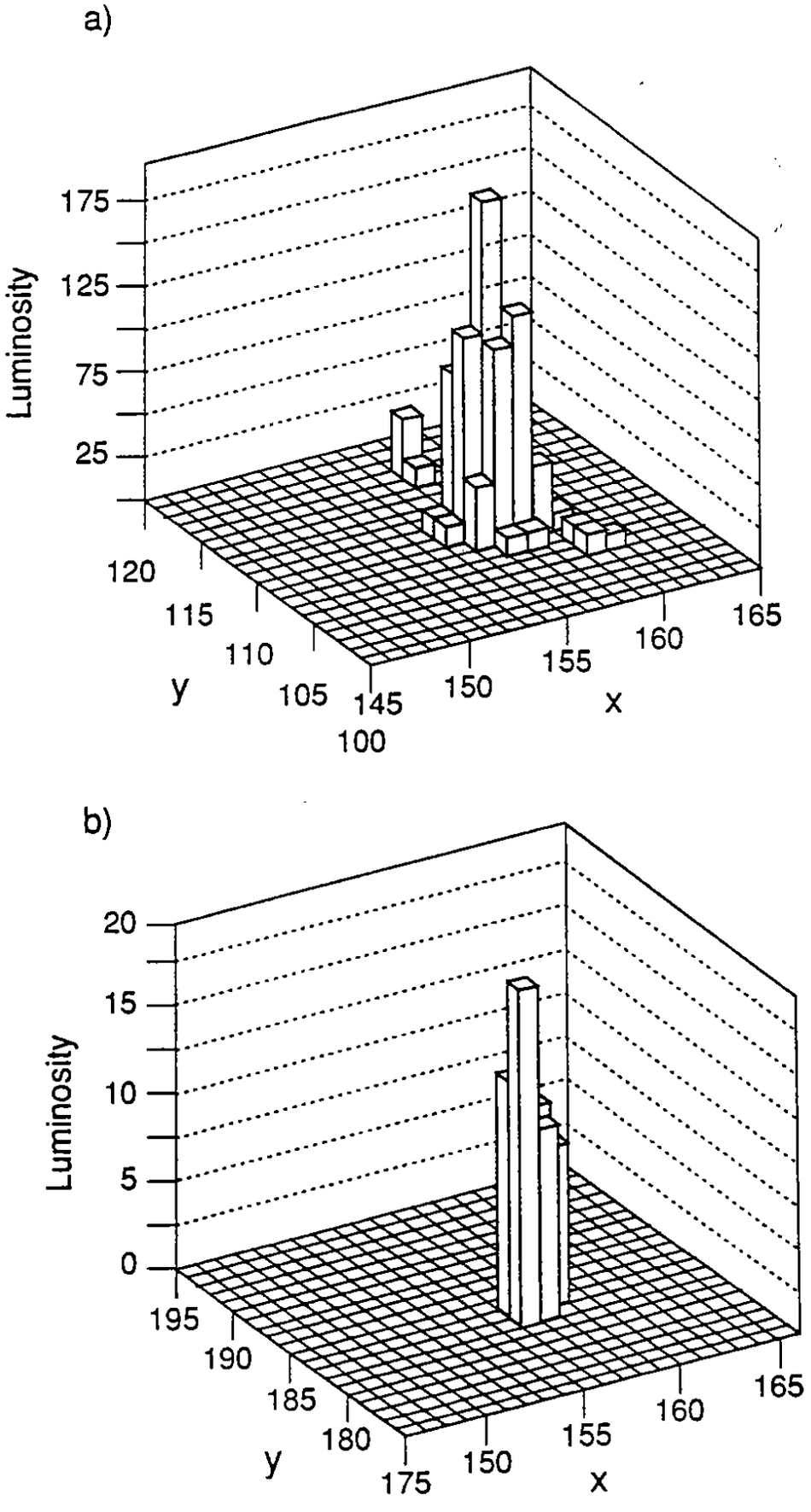
a)
Luminosity
175
125
75
25
120
115
110
105
100
y
145
150
155
160
165
x
b)
Luminosity
20
15
10
5
0
195
190
185
180
175
y
150
155
160
165
x

Fig. 9

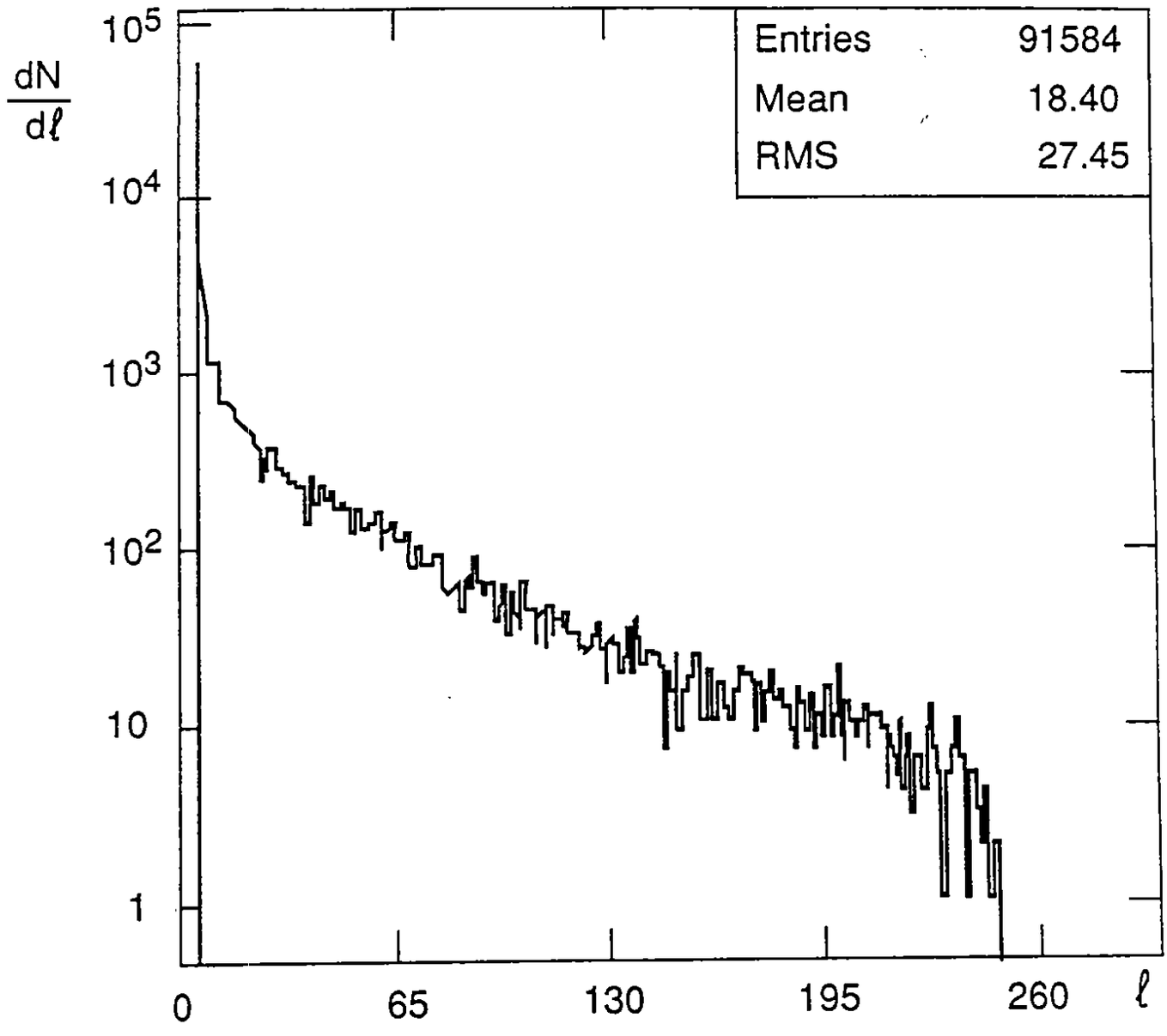
dN/dℓ
10^5
10^4
10^3
10^2
10
1
0
65
130
195
260
ℓ
Entries 91584
Mean 18.40
RMS 27.45

Fig. 10

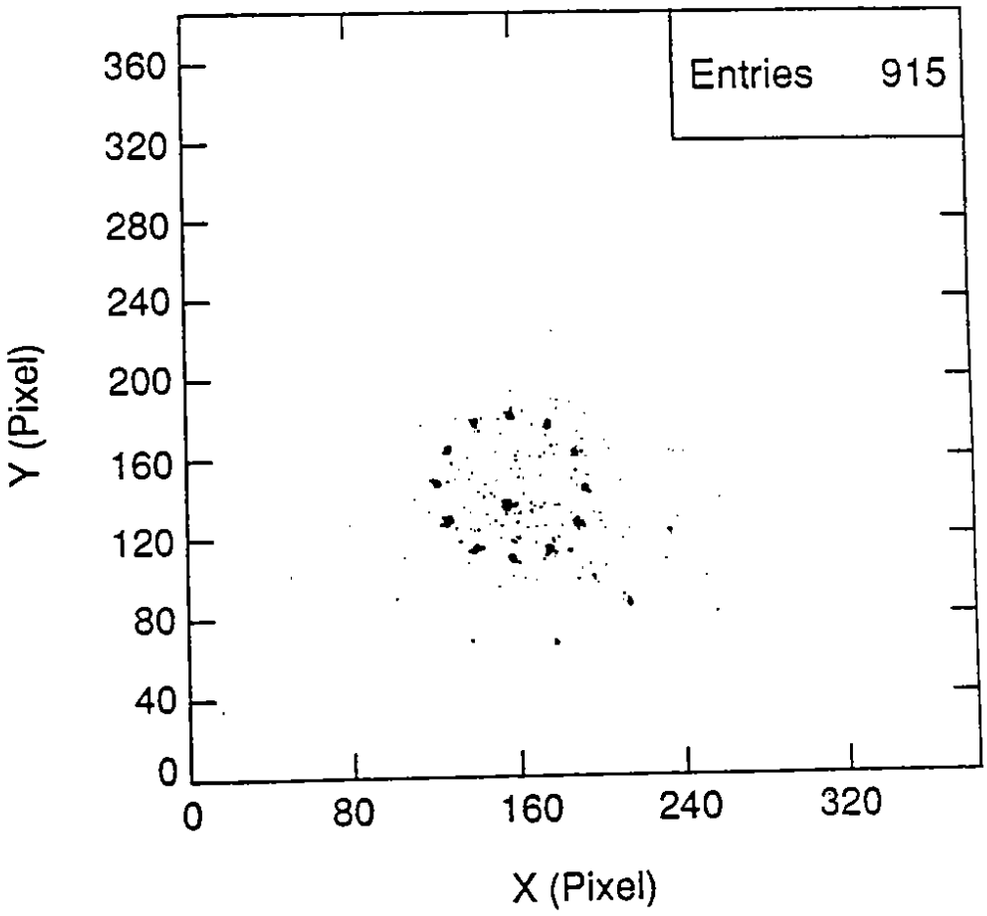
Entries 915
360
320
280
240
200
160
120
80
40
0
0
80
160
240
320
Y (Pixel)
X (Pixel)

Fig. 11

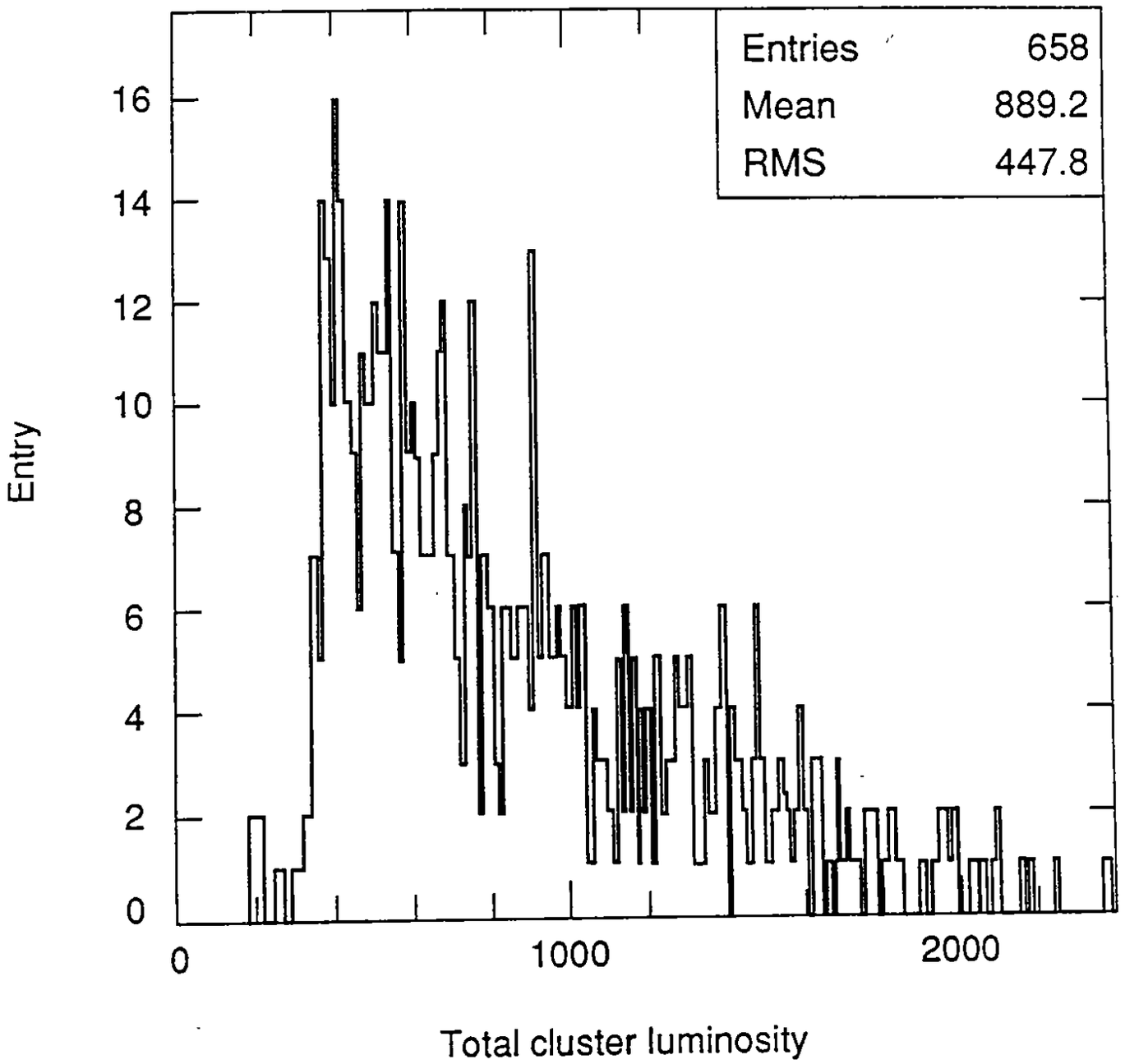
Entries 658
Mean 889.2
RMS 447.8
Entry
16
14
12
10
8
6
4
2
0
0
1000
2000
Total cluster luminosity

Fig. 12

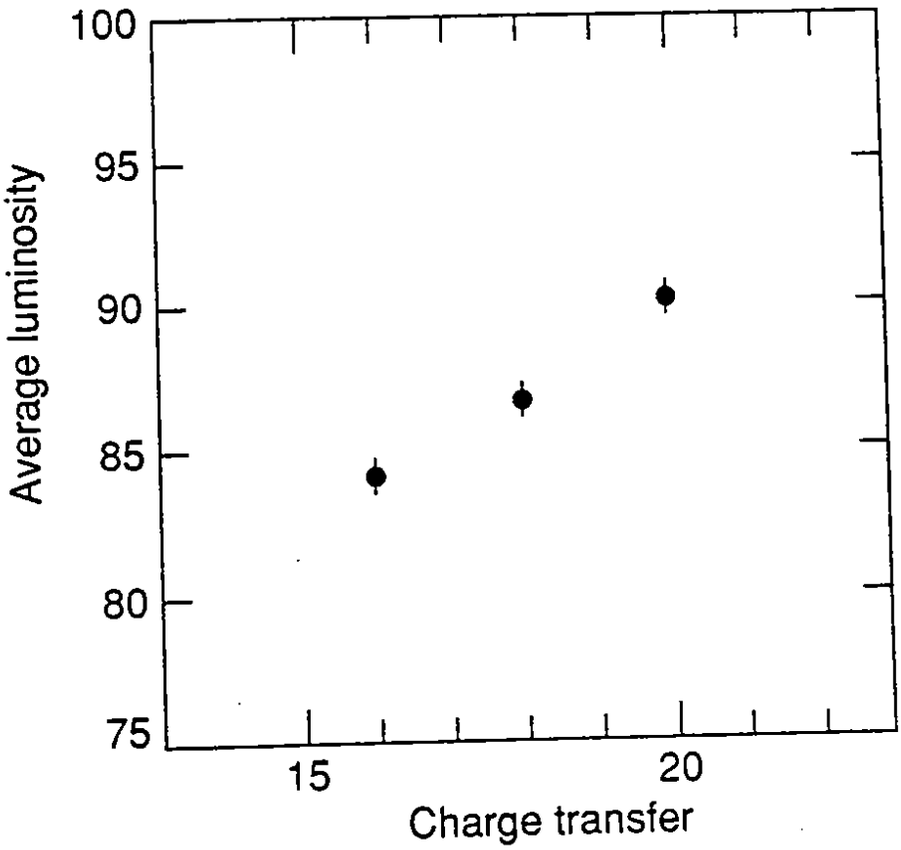

Fig. 13

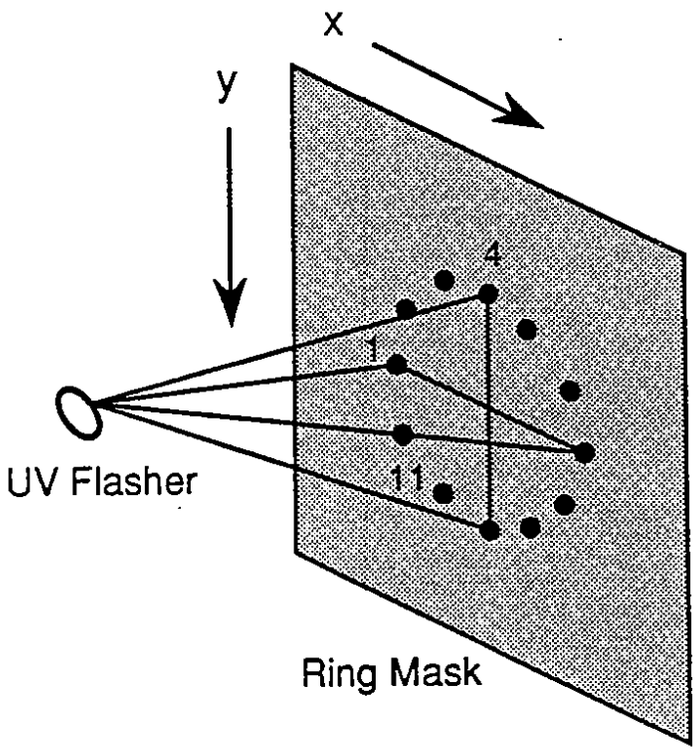

Fig. 14

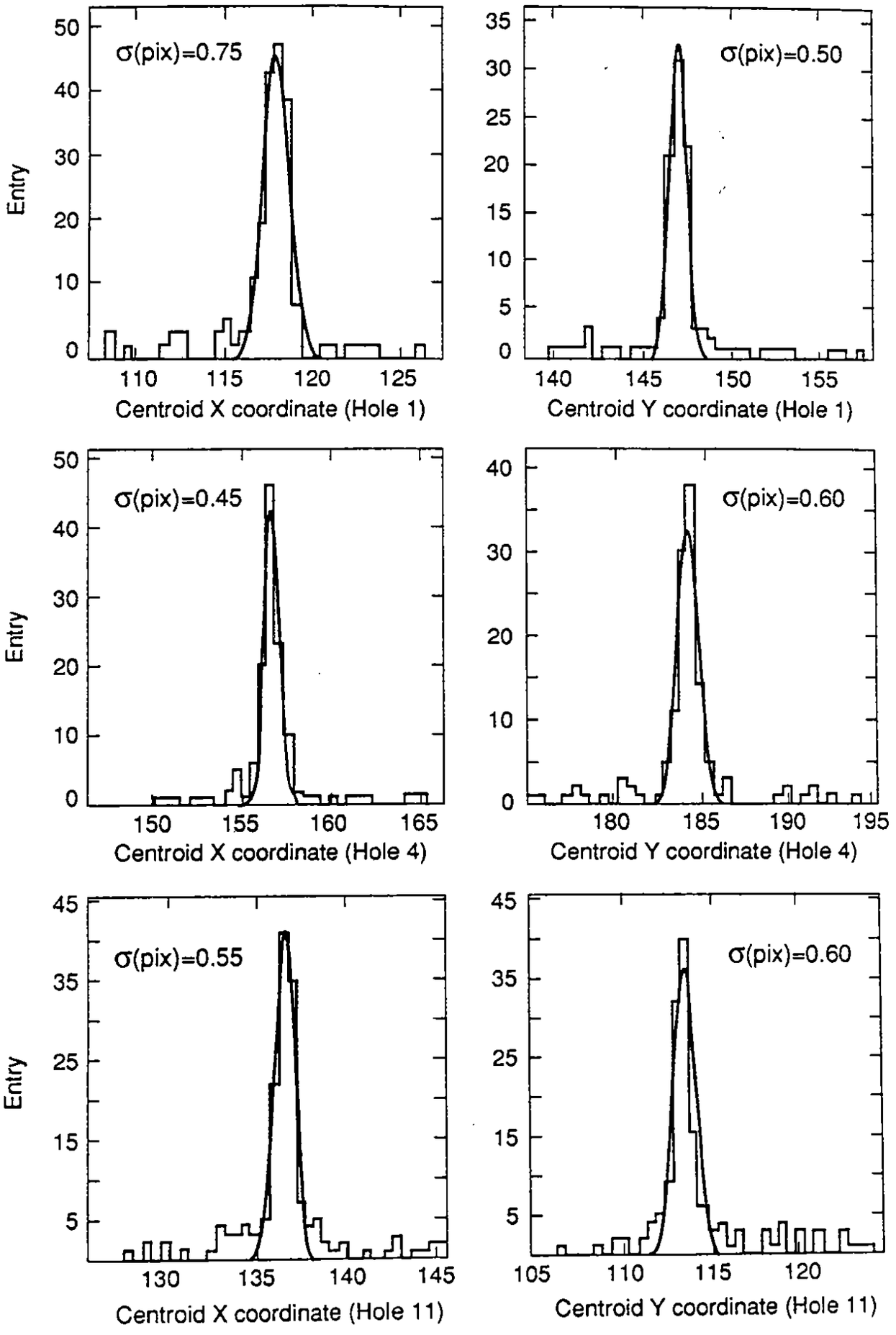
σ(pix)=0.75
Entry
Centroid X coordinate (Hole 1)
σ(pix)=0.50
Centroid Y coordinate (Hole 1)
σ(pix)=0.45
Centroid X coordinate (Hole 4)
σ(pix)=0.60
Centroid Y coordinate (Hole 4)
σ(pix)=0.55
Centroid X coordinate (Hole 11)
σ(pix)=0.60
Centroid Y coordinate (Hole 11)

Fig. 15

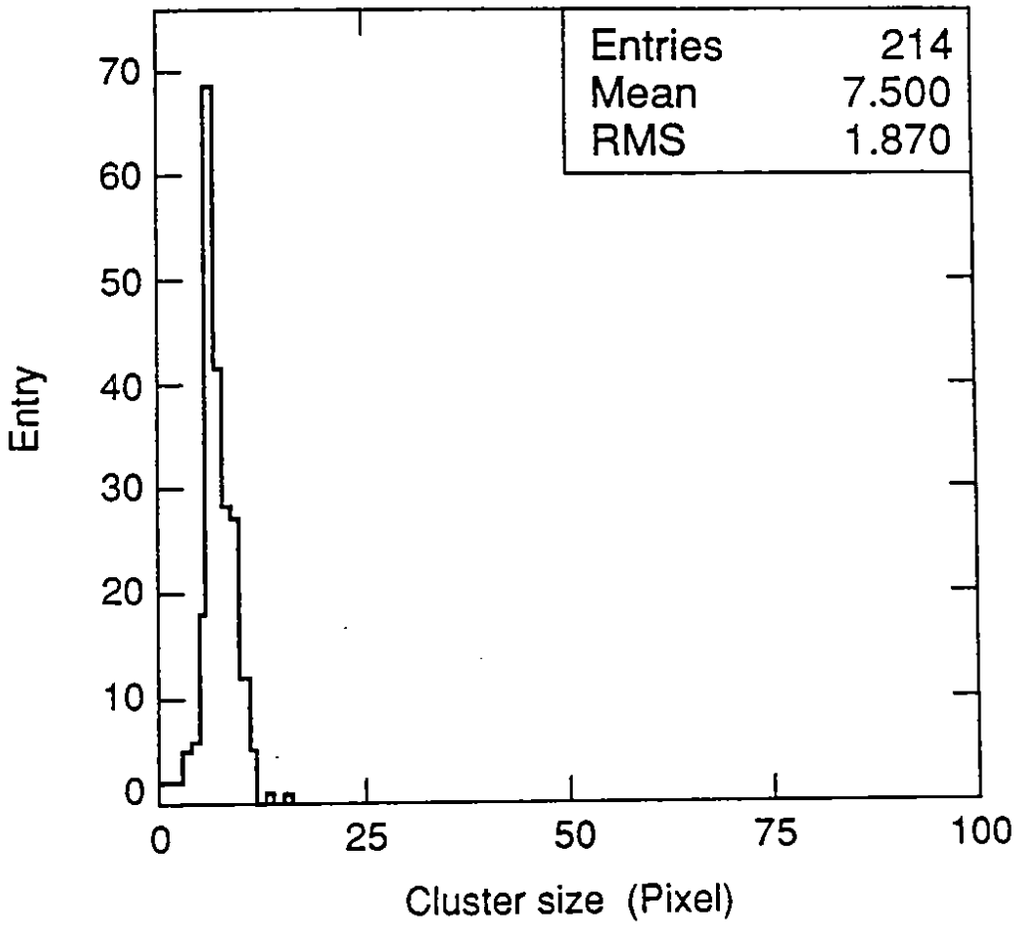
Entries 214
Mean 7.500
RMS 1.870
70
60
50
40
30
20
10
0
Entry
0
25
50
75
100
Cluster size (Pixel)

Fig. 16